Novel EMIC Wave Propagation Pathway Through Buchsbaum Resonance and Inter-Hemispheric Wave Interference: Swarm Observations and Modelling

Ivan Pakhotin[1,1], Ian Mann[2,2], Dmytro Sydorenko[2,2], and Robert Rankin[2,2]

[1]University of Calgary
[2]University of Alberta

November 30, 2022

Abstract

In-situ conjugate electromagnetic ion cyclotron (EMIC) waves observed by the Swarm mission in both hemispheres are presented. A complex and unusual pattern of Alfvénic EMIC wave energy is observed, with a mid-latitude peak close to the source at L=3.3, as well as a secondary lower L-peak. A wave propagation model reveals that the secondary peak at L=1.7 may be explained by wave power being redirected equatorward due to the Buchsbaum resonance, crossing and interfering with the same EMIC wave power propagating equatorwards from the opposite hemisphere. This interference creates a coherent equatorial driver for a low-L field line resonance at the secondary peak, and which is associated with strong shear-to-fast mode coupling in the ionosphere. This behavior complicates the interpretation of low-Earth orbit EMIC data for applications assessing radiation belt loss. Combined LEO observations and modelling enable these novel and localized magnetosphere-ionosphere EMIC wave propagation pathways to be identified.

Novel EMIC Wave Propagation Pathway Through Buchsbaum Resonance and Inter-Hemispheric Wave Interference: Swarm Observations and Modelling

I. P. Pakhotin[1, 2], I.R. Mann[1], D. Sydorenko[1], R. Rankin[1]

[1] Department of Physics, University of Alberta, Edmonton, Alberta, Canada

[2] Department of Physics and Astronomy, University of Calgary, Calgary, Alberta, Canada

Key Points

- EMIC wave propagation from the magnetosphere to the ionosphere is complicated by reflection from the Buchsbaum resonance and interference
- Waves reflected from the Buchsbaum resonance interfere to generate a coherent driver for a secondary lower latitude field line resonance
- This generates a field-guided secondary lower-latitude peak associated with strong shear-to-fast mode energy conversion in the ionosphere

Abstract

In-situ conjugate electromagnetic ion cyclotron (EMIC) waves observed by the Swarm mission in both hemispheres are presented. A complex and unusual pattern of Alfvénic EMIC wave energy is observed, with a mid-latitude peak close to the source at L=3.3, as well as a secondary lower L-peak. A wave propagation model reveals that the secondary peak at L=1.7 may be explained by wave power being redirected equatorward due to the Buchsbaum resonance, crossing and interfering with the same EMIC wave power propagating equatorwards from the opposite hemisphere. This interference creates a coherent equatorial driver for a low-L field line resonance at the secondary peak, and which is associated with strong shear-to-fast mode coupling in the ionosphere. This behavior complicates the interpretation of low-Earth orbit EMIC data for applications assessing radiation belt loss. Combined LEO observations and modelling enable these novel and localized magnetosphere-ionosphere EMIC wave propagation pathways to be identified.

Plain Language Summary

Electromagnetic ion cyclotron (EMIC) waves are important in near-Earth space due to their role in reducing the amount of radiation in the Earth's radiation belts following geomagnetic storms. They are studied using satellites and ground observatories. Our paper reveals how these waves can follow complicated and previously unknown pathways to reach the upper atmosphere where they can be detected on the ground. This study shows a new and unusual effect where some EMIC wave energy is reflected and diverted towards the equator, where it meets its opposite-hemisphere counterpart, interferes with it and sets up a resonance. This resonance then creates a new signal peak in the upper atmosphere at lower latitudes, far away from the location of the initial source. This presents a new and hitherto unseen pathway for wave energy to travel from their generation region in near-Earth space down to the ionosphere.

Understanding such pathways is very important for correctly diagnosing the location of these wave populations in space, and assessing their role in causing reductions in the levels of space radiation.

Index Terms

2487 Wave propagation, 2494 Instruments and techniques, 2736 Magnetosphere/ionosphere interactions, 2768 Plasmasphere, 2753 Numerical modeling

Keywords

EMIC waves, magnetosphere, ionosphere, wave reflection, Buchsbaum resonance, field-line resonances

1. Introduction

Electromagnetic ion cyclotron (EMIC) waves are important instabilities linked with rapid radiation belt dropouts (Shprits et al., 2008). Their importance in radiation belt dynamics is an active area of research and debate (e.g. Millan and Thorne, 2007, Shprits et al., 2013, 2018; Mann et al., 2016, 2018). It is also known that EMIC waves can be spatially and temporally localised (Usanova et al., 2010, Blum et al., 2016, 2017; Hendry et al., 2020; Kim et al., 2018a, Kim et al., 2020) and can propagate in the Earth-ionosphere waveguide (e.g., Mann et al., 2014 and references therein). This presents a dilemma in how to effectively observe them.

Ground magnetometer stations (e.g. Mann et al., 2008) can provide continuous monitoring but are fixed in position and their signatures are complicated by ionospheric ducting (e.g. Mann et al., 2014, Kim et al., 2018b and references therein). Meanwhile, high-apogee spacecraft in elliptical orbits, e.g. Van Allen Probes, Cluster, or MMS, provide limited temporal coverage as they can rapidly cross the narrow L-shells supporting the EMIC waves (e.g. Usanova et al., 2008) and only return to the same region on relatively long orbital timescales.

Meanwhile, polar low-Earth orbit (LEO) satellites, such as the European Space Agency (ESA) Swarm (Friis-Christensen et al., 2008) mission, cross L-shells rapidly and thus offer the possibility of higher temporal coverage. For example, Swarm A and C cross the same L-shell up to four times in only 90 minutes. This makes LEO satellites potentially attractive platforms for studying EMIC waves.

The pathway by which EMIC waves propagate from their source region to ground can be complex, often involving polarization reversal, deflections at the Buchsbaum resonance (Buchsbaum, 1960), mode conversion (e.g., Kim and Johnson, 2016), ionosphere waveguide ducting, and possible reflection around equatorial plasma bubbles (Kim et al., 2018b). Inner magnetosphere propagation models (e.g. Sydorenko and Rankin, 2012, 2013) may be used to understand the correspondence between low-altitude and ground EMIC signatures and their source locations farther out in the magnetosphere. These models need to be validated against empirical measurements. Here we use a novel model for EMIC wave propagation to demonstrate the importance of the Buchsbaum resonance in affecting the pathways by which EMIC waves reach the ionosphere within the inner magnetosphere. Whereas Kim and Johnson (2016) demonstrated how the Buchsbaum resonance can affect wave dynamics near their equatorial generation region at L~7, here we use a simulation domain which covers the entire magnetosphere-ionosphere domain and reveal an unexpected new pathway by which EMIC wave energy may reach the ionosphere at lower-L.

We combine data from Swarm A and C with results from this wave propagation model. Two EMIC wave signal power peaks at LEO are identified in both hemispheres. The primary high-latitude peak (L~3.3) appears to represent EMIC wave power travelling straightforwardly down the field line to the ionosphere. The secondary peak (L~1.7) appears to have been generated from the same source, travelling along a novel pathway from the magnetosphere to the ionosphere which to our knowledge has not been reported previously. The model results show compelling evidence for EMIC wave reflection through Buchsbaum resonance, followed by the two reflected waves, one from each hemisphere, crossing at the equator and interfering to set up resonant standing waves which pump energy into a field-line resonance (FLR), which is observed as the secondary peak. Multi-spacecraft phase differencing reveals that the secondary peak appears to feature strong shear-to-fast wave mode conversion.

2. Data and Instrumentation

The ESA Swarm mission (Friis-Christensen et al., 2008) was launched into a low-Earth polar ~87° orbit in 2013 and consists of three identical satellites. Swarm A and C form a pair travelling at 450 km altitude with a separation of 1.4° in latitude and a varying along-track separation that is ~10 seconds apart at the time of the event. All spacecraft are equipped with the Vector Fluxgate Magnetometers (VFM) sampling the magnetic field at 50 Hz (Olsen et al., 2013). The coordinate system used here is the spacecraft coordinate system (VFM) where VFM_1 faces in the direction of the spacecraft motion, VFM_3 faces radially upwards away from Earth, and VFM_2 faces azimuthally and completes the triad. The Langmuir Probes provide plasma density estimates at 16 Hz (Knudsen et al., 2017).

The Van Allen Probes pair were launched in 2012 into near-equatorial elliptical orbits with an apogee of ~37,000 km and a perigee of ~600 km (Kessell et al., 2012). The magnetic field instrument has a sampling rate of 64 samples/sec and forms part of the Electric and Magnetic Field Instrument Suite (EMFISIS) (Kletzing et al., 2013).

The Canadian Array for Real-time InvestigationS of Magnetic Activity (CARISMA) ground-based magnetometer network (Mann et al., 2008) consists of an array of induction coil magnetometers (ICM) and fluxgate magnetometers (FGM), measuring magnetic field perturbations on the ground across western Canada and the northern United States. The ICMs and FGMs sample at 100 Hz and 8 Hz respectively.

3. Results

3.1 Event Observations

Swarm A/C traversed an area of intense EMIC wave activity on 17th September 2015, 10-11 UT. The pair flew northwards on the nightside through a conjugate region of EMIC wave activity spanning the southern and northern sub-auroral regions. EMIC waves (~1.5 Hz) were detected simultaneously on several CARISMA groundstations and on Swarm A/C. On Swarm, the waves were detected in both the quasi-azimuthal B_VFM_2 and |B| components. Phase differencing (Balikhin et al., 1997, Pakhotin et al., 2013) was used to estimate the source region of the compressional disturbance assuming the source location does not change on the timescale needed to traverse the area of interest, and assuming that the propagation speed of the compressional component away from the source in the duct is locally homogeneous. Figure 1 displays the results of the analysis for both hemispheres. The intersection of the two black solid lines in Figure 1 (a), tracing the vectors of maximum and zero phase difference in the compressional magnetic field, allows the triangulation of the signal source, marked with a black cross. Dashed black lines denote the hypothetical isolines of compressional wave power spreading isotropically from the source. The same analysis has been applied to the southern hemisphere (Figure 1 (b)). The intersection in that hemisphere is close to the theoretical magnetic conjugate point, calculated using the IRBEM library, which is also marked as a black cross. Additional analysis assessing the impacts of potential latitudinally non-uniform propagation speeds is presented in Supplementary Material Figure S1, based on Swarm densities inferred from the Swarm Langmuir probe. However, the resulting difference in the inferred source L-shell is small.

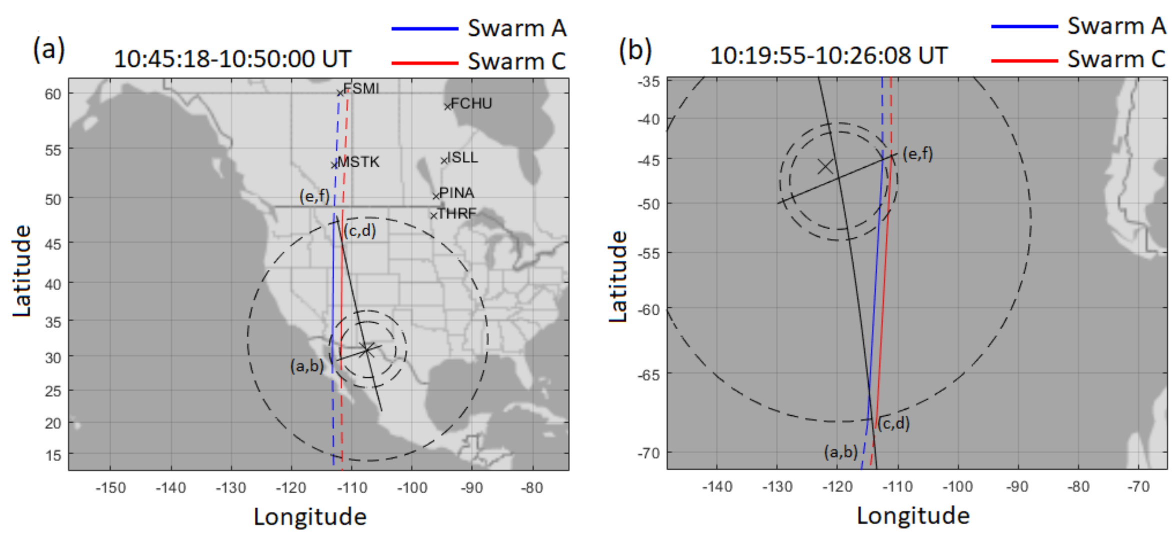

Figure 1: Northern (a) and southern (b) hemisphere tracks for Swarm A (SwA; blue), and Swarm C (SwC; red). Black solid lines denote straight lines drawn between SwA and SwC inter-spacecraft separation vectors at the times of maximum and zero phase differences. The intersection of these lines gives the approximate compressional source location. The blue and red traces are solid while Swarm A and C traversed the area between these zero-phase and max-phase locations, and dashed otherwise. Black dashed circles represent wavefronts assumed

to be spreading out omni-directionally from the source. Smaller black crosses denote CARISMA groundstations. Large black crosses denote intersection points of the phase lines (a) and its magnetically conjugate location (b). In the left panel, the small letter pairs (a,b), (c,d) and (e,f) refer to the corresponding-letter panels in the waveforms shown in Figure 3 for the northern hemisphere; in right panel the same letter pairs refer to the panels in Supplementary Figure S3 for the south.

In both hemispheres, the compressional wave power appears to originate from L ~ 1.7. In general, EMIC waves are not expected to be observed equatorially at such low L-shells (Saikin et al., 2015). Van Allen Probe B (VAP-B) passed close to Swarm A/C in the equatorial plane around 1021 UT and neither Swarm A/C nor VAP-B observed any equatorial EMIC wave activity at 1.5 Hz (see Supplementary Figure S2). VAP-B, which moves in the azimuthal direction due to its near-equatorial orbit, also did not see wave activity before or afterwards, despite being at higher L-shells. This suggests that the event was azimuthally localized.

In Figure 2 (a), high-pass filtered B_VFM_2 data shows large-scale auroral-zone FACs between ~1009-1018 UT in the south and ~1050-1056 UT in the north. The magnetic perturbations related to EMIC waves are highlighted with green boxes, shown in more detail in Figure 2 (b) where the magnetic field data has been processed with a 10s-window high-pass filter to bring out the Pc1 band signal. Assuming that the plasmasphere ends where relatively large FACs begin (e.g. Heilig and Lühr, 2018), the plasmapause location for both hemispheres would be around L ~4.7-4.8. Similarly, estimations obtained from the VAP-B EMFISIS instrument (Kletzing et al., 2013), utilizing the upper hybrid frequency and density, would place the plasmapause at L ~ 5-5.2. These considerations would then place the Pc1 signal maxima inside the plasmasphere at L ~3.3 in both hemispheres. This agrees with prior studies (e.g. Kim et al., 2018a) which show EMIC waves on Swarm to be a sub-auroral phenomenon.

Figure 2 (c) and (d) show the transverse (B_VFM_2) and compressional (|B|) components of the magnetic field in the frequency domain. The ~1.5 Hz waves are clearly seen in both components, strongly suggesting in-situ mode conversion from the shear Alfvén to the compressional mode. Interestingly, while the maximum wave power in the shear Alfvén mode (Figure 2 (c)) appears near the assumed source location at L~3.3 (~1021 UT in the south and ~1050 UT in the north), there is also a secondary signal extending to lower latitudes in both hemispheres. The maximum of this secondary signal is around 1025 UT in the south and around 1045 UT in the north. The secondary signal is marked in Figure 2 (b) with orange boxes. In both hemispheres, wave power drops between the primary and secondary signals. The secondary signal is also pronounced in the compressional component (Figure 2 (d)). The maximum wave intensities of the primary peaks, in both hemispheres, are around L ~ 3.3. The maximum intensities of the secondary peaks are at L ~ 1.7-1.8 in both hemispheres, which agrees with the earlier geometric analysis in Figure 1 placing the secondary compressional Pc1 wave power source at L ~ 1.7.

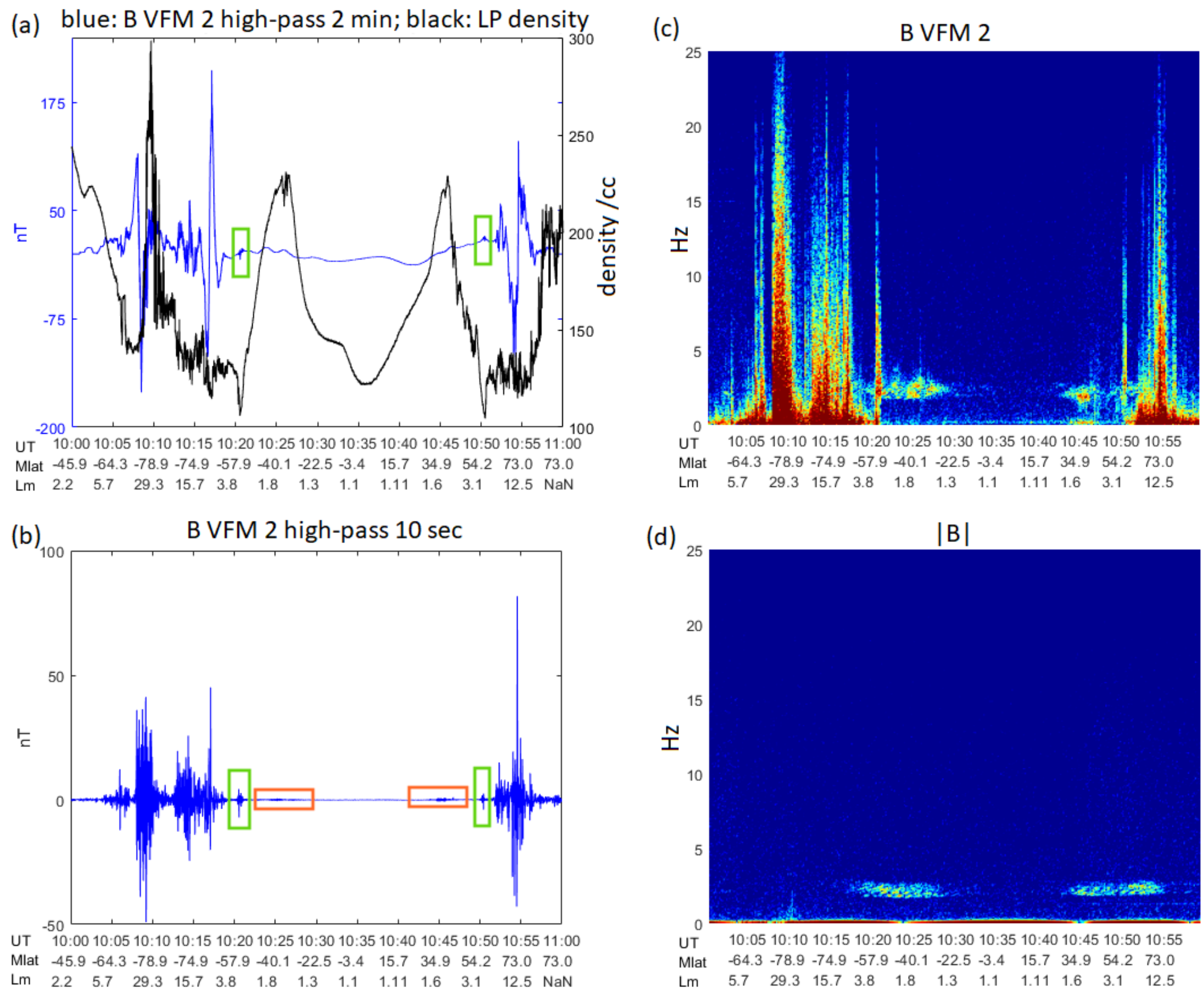

Figure 2: For 17 Sept 2015, 10:00:00-11:00:00 UT, (a) blue shows the time series of B_VFM_2 after the application of a 2-minute moving average high-pass filter (in nT); black shows Langmuir probe density, (b) shows the B_VFM_2 signal high-pass filtered with a 10-second moving average. The primary signal intensity maxima are marked in (a) and (b) with green boxes, further the secondary intensity maxima are marked on (b) with orange boxes. (c) and (d) show dynamic power spectra of B_VFM_2 and the B-modulus, respectively.

The phase differencing methodology in the ionosphere for the secondary peak is demonstrated in detail in Figure 3, which shows the |B| readings on the spacecraft pair for three time periods. Figure 3 (a) and (b) show the magnetic perturbations around 1045 UT, where the wavepackets arrive at Swarm C before Swarm A. During the second time period, around 1050 UT (Figure 3 (c) and (d)), the wave peaks from Swarm A and C are in phase, meaning that both observe the wave simultaneously. Finally, during the third time period, around 1052 UT, shown in Figure 3 (e) and (f), the lagging Swarm A observes the wave before Swarm C, meaning that the wavefronts are now catching up with the satellite pair. Similar geometric calculations were performed for the southern hemisphere (Supplementary Figure S3). In both hemispheres, the inter-spacecraft wave phase changes smoothly between the three time periods, without evidence of phase wrap (Supplementary Figure S4). The magnetically conjugate emission regions are to the left of Swarm A/C in the south, and to the right of Swarm A/C in the north, consistent with conjugate field line tracing.

Meanwhile, most CARISMA ICMs observe significant wave power at ~1.5 Hz around the time of the Swarm traversals and for several hours afterwards (see Figure S5). The wave signal-to-noise ratio increases with decreasing ground station latitude, suggesting that the signal source is either close to THRF (L=3.6) or southwards of it. The same wave signal is also detected on other CARISMA FGM stations such as Pinawa (PINA; L=4.1) and Osakis (OSAK; L=3.2), the amplitudes being consistent with the L-shell of the primary wave inferred on Swarm.

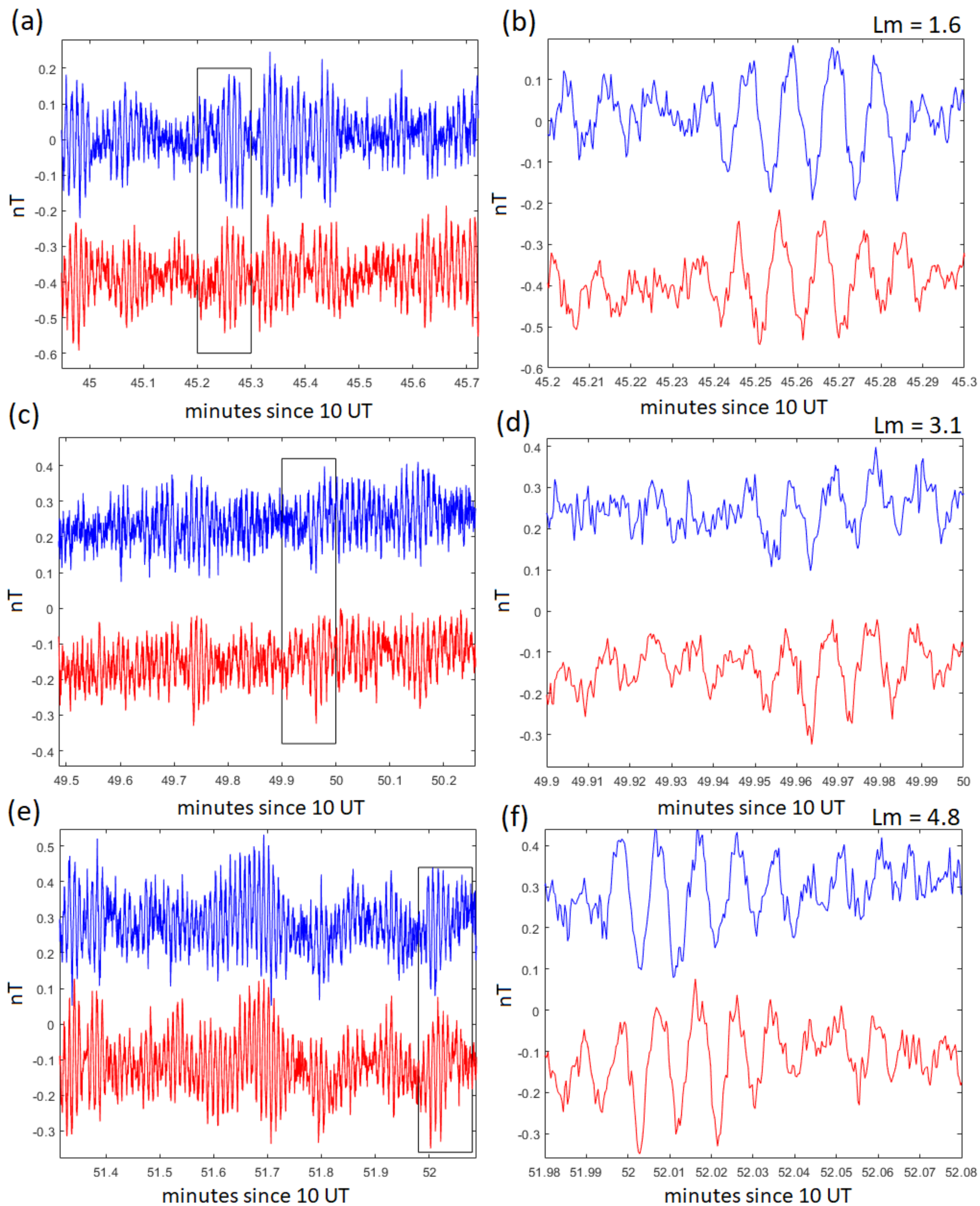

Figure 3: B-field modulus readings for three time periods on Swarm A (blue) and Swarm C (red) as they traversed the northern hemisphere, the two time series being offset by 0.4 nT for easier viewing. The right column shows the areas highlighted by the black squares in the left column. Specifically, (a) and (b) show the period of maximum phase difference between Swarm A and C in the northern hemisphere, (c) and (d) show the zero-phase period, (e) and (f) show the period where Swarm A sees each wave front before Swarm C.

3.2 Simulation Results

The event described in the present paper is simulated using a two-dimensional linear numerical model of ultra-low frequency (ULF) wave propagation in atmosphere, ionosphere, and magnetosphere. Equations solved by the model are presented in Supplementary Text S1.

The simulation domain is a sector in the plane of a magnetic meridian, with the magnetic latitude ranging from -80° to 80°. Spatial resolution in the radial and meridional directions is 10 km at the Earth surface. The inner and outer radii of the simulation domain are 6,380 km and 60,000 km, respectively. The ionosphere in the simulation begins at an altitude of 110 km. The azimuthal wavenumber is assumed to be 40, based on the assumed azimuthal scale size of a localized EMIC wave source. Parameters of ionosphere, magnetosphere, and thermosphere are set using two-dimensional profiles of ion, electron, and neutral densities and temperatures provided by IRI (Bilitza, 2018), GCPM (Gallagher et al, 2000), and MSIS (Hedin, 1991) for the 17th of September 2015, universal time 11 hours, magnetic local time 4.25 hours.

The wave source is an electric current loop in the meridional plane, 500 km long in the radial direction and with latitudinal boundaries at ±0.5°, positioned at a radius of 20,000 km in the equatorial plane. The period of current oscillations in the wave source is 0.5 seconds. The amplitude grows linearly for 10 seconds and then remains constant. The specific value of the current amplitude in the source is of no importance since the wave model is linear. The whole simulation lasts for 45 seconds. In most of the domain, the wave amplitude reaches its stationary level after about 30 seconds since the beginning of the simulation.

Two metrics are used below to describe compressional and torsional Alfvén waves. The azimuthal magnetic field perturbation, B_φ, which is normal to the dipole geomagnetic field and therefore contributes to the variation of the magnetic field vector's direction, characterizes the torsional wave. The difference between the modulus of the full magnetic field (the sum of the wave perturbation $\vec{B}$ and the geomagnetic field $\vec{B}_0$) and the modulus of the geomagnetic field, $\delta|B| \equiv \sqrt{\left(\vec{B}+\vec{B}_0\right)^2 - \vec{B}_0^2}$, characterizes the compressional wave. Note that two movies showing evolution of B_φ and $\delta|B|$ in space and time during the simulation are provided in Supplementary Materials.

The spatial profile of the ion density is strongly non-uniform and includes a relatively dense plasmasphere as well as a depleted plasma outside it, as shown in Figure 4(c). The wave source is inside the plasmasphere. The source excites both torsional and compressional waves. The torsional waves propagate along the geomagnetic field, see Figure 4(b). The compressional waves propagate across the geomagnetic field, mostly towards the boundary of the plasmasphere, see Figure 4(a). Compressional waves emitted by the source are ducted between surfaces $\omega = \omega_{c,O}$ and $\omega = \omega_{bb}^{+}$, where ω is the wave frequency, $\omega_{c,O}$ is the cyclotron frequency of O^+ ions, and ω_{bb}^{+} is a Buchsbaum resonance frequency, see the region between the magenta and the blue curves in Figure 4(a). Buchsbaum resonance frequencies $\omega_{bb}^{\pm}$ are calculated for a 3 component plasma (H^+, He^+, O^+) using equation (13) of (Barbosa, 1982), the plus or minus in the superscript of $\omega_{\mathrm{bb}}^{\pm}$ corresponds to using the plus or minus in this equation, respectively. Note that ω_{bb}^{+} is close to the cyclotron frequency of He^+ ions $\omega_{c,He}$, compare the blue and cyan curves in Figures 4(a), 4(b). In the northern hemisphere, compressional waves impinging on the plasmaspheric boundary transform into waves with significant torsional component propagating along the boundary on the outer side of the plasmasphere. Such a process does not occur at the plasmaspheric boundary in the southern hemisphere, see Figures 4(a) and 4(b). The difference may be related to the magnitude of the density gradient at the plasmaspheric boundary which is noticeably sharper in the northern hemisphere, as shown in Figure 4(c). Waves outside the plasmasphere propagating away from the Earth are beyond the scope of the present paper.

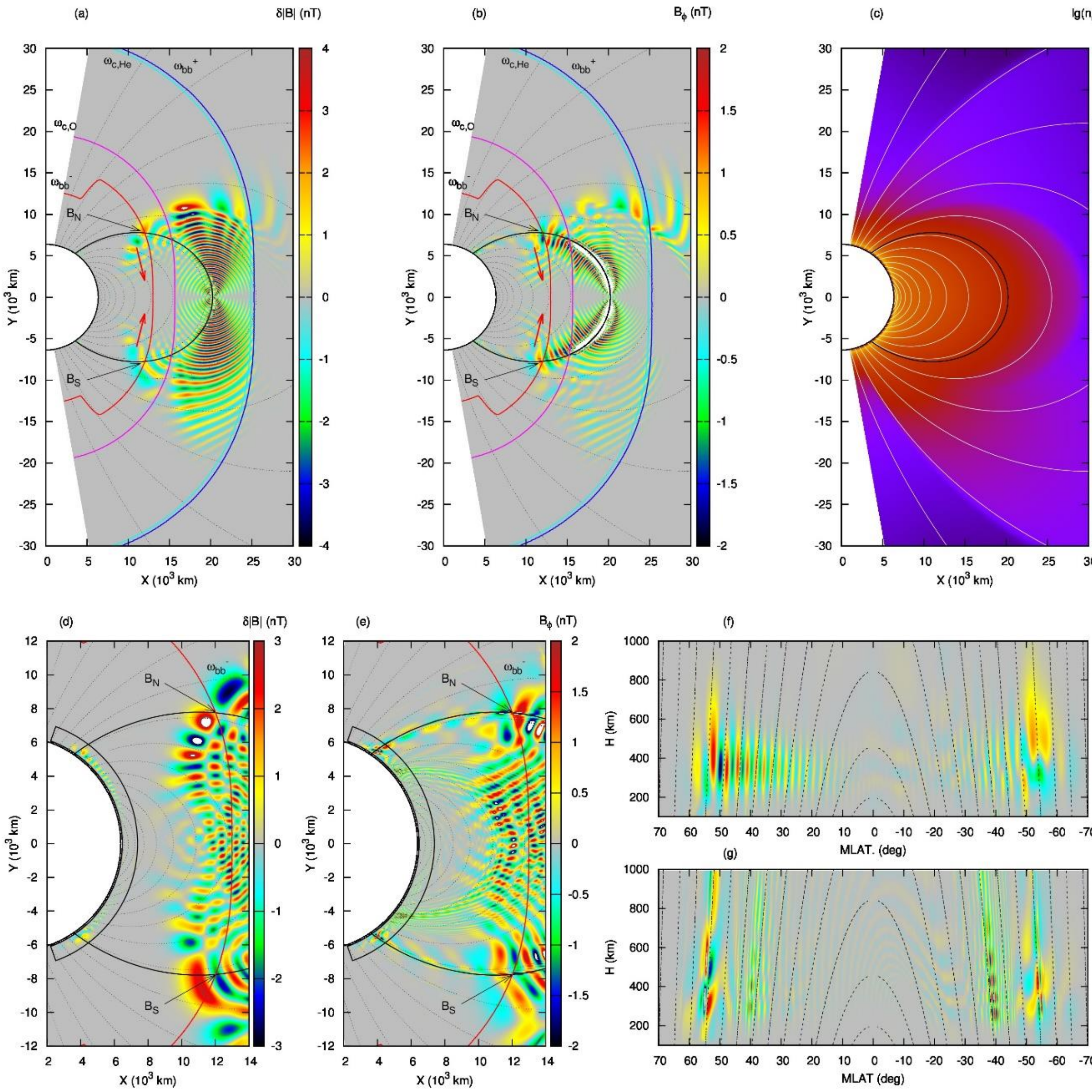

Figure 4: Simulation results. Snapshots of the perturbation of the full magnetic field modulus (a) and the wave azimuthal magnetic field (b) at time t=14.375 sec; electron density (c); perturbation of the full magnetic field modulus (d,f) and the wave azimuthal magnetic field (e,g) at time t=35.997 sec. In (a,b,c,d,e), the black curve is the field line passing through the wave source in the equatorial plane. Gray curves in (a,b,d-g) and white curves in (c) represent dipole field lines crossing the Earth surface at latitudes of 80° to 10° with a 5° step. In (a,b), the Buchsbaum resonance surfaces $\omega = \omega_{bb}^{\mp}$ are shown by red (ω_{bb}^{-}) and blue (ω_{bb}^{+}) curves; surfaces $\omega = \omega_{c,O}$ and $\omega = \omega_{c,He}$ are shown by the magenta and cyan curves, respectively. In (d,g), red curves mark surfaces $\omega = \omega_{bb}^{-}$. In (a,b,d,e), black arrows and labels B_N and B_S mark locations of Buchsbaum resonances $\omega = \omega_{bb}^{-}$ on the field line of the wave source in the northern and southern hemispheres, respectively. In (a,b), red arrows mark equatorward propagating waves excited at locations $B_{N,S}$. Regions of (f,g) match the spherical slabs shown in (d,e); the horizontal and vertical coordinate axes in (f,g) are the latitude and altitude.

Torsional waves generated by the source and propagating towards the ionosphere along the geomagnetic field reach points of Buchsbaum's resonance $\omega = \omega_{bb}^{-}$ about 10.7 seconds after the beginning of simulation. In Figure 4, these points are labelled B_N and B_S in the northern and southern hemispheres, respectively. In the vicinity of these points, mode conversion occurs and waves propagating towards the equatorial plane appear, see the regions around the red arrows in Figures 4(a) and 4(b). Meanwhile, the original torsional wave continues its propagation along the field line of the source (black curve in Figure 4) into the ionosphere, see Figure 4(b). After about 12.2 seconds, two primary channels of wave energy entering the ionosphere form, one in each hemisphere, at magnetic latitude of about 55° north and south, respectively, see Figures 4(b), 4(e), and 4(g).

Torsional waves in the primary wave channels excite compressional waves in the lower ionosphere propagating equatorward inside the ionospheric waveguide, with most of the wave energy confined below the altitude of about 600 km, see Figures 4(d, f). The excitation is more efficient in the northern hemisphere (Figure 4 (f)), probably due to different polarization of waves in the northern and southern primary channels. Meanwhile, the equatorward propagating waves emitted from points of Buchsbaum resonance $B_{N,S}$ excite oscillations along field lines entering the Earth surface at latitudes about 40°, see Figures 4(e) and 4(g). These oscillations are standing torsional Alfvén waves, the compressional component is very weak, compare figures 4(d,f) and 4(e,g). They form two secondary channels of wave energy entering the ionosphere, one in each hemisphere, at time of about 20.5 seconds.

4. Discussion

The model results presented here demonstrate a new pathway for EMIC wave propagation from a higher-L magnetosphere source to the low-L ionosphere. This pathway is generated due to Buchsbaum resonance effects which reflect waves back into the lower-L magnetosphere. These reflected waves interfere, creating a coherent equatorial Alfven wave driver which generates a separate peak in EMIC wave power at lower L. Whilst Kim and Johnson (2016) showed how the Buchsbaum resonance can affect EMIC wave propagation at high latitudes, to our knowledge our work is the first to demonstrate the importance of the Buchsbaum resonance in channeling EMIC wave energy to the ionosphere.

Two pairs of wave channels are observed both in the model and in Swarm data – a primary at ±56° magnetic latitude (MLAT) and a secondary at ±38° MLAT. Beyond 60° MLAT – the model plasmaspheric boundary – the shear wave does not propagate. Swarm estimates place the plasmapause ~61° MLAT. Near-equatorial wave amplitudes below 2000 km are negligible both in the model and in the Swarm/VAP-B data.

It is not clear why, in the model, the secondary wave channels are not as efficient in compressional wave excitation as the primary channels are; additional studies are needed. One possible reason may be relatively large transverse and parallel wavenumbers in the secondary channels, see Figure 4(g). Interestingly, it appears from multi-satellite wave vector analysis

(Figures 1, 3, S1, 4) that it is the secondary peak which acts as the primary wave source for compressional waves. This may be due to the fact that at lower latitudes, magnetic field lines are more tilted, which may increase shear-to-fast mode conversion efficiency (e.g. Sciffer et al., 2004).

5. Conclusions

Multiple studies report on the complex relationship between space and ground Pc1 pulsations (e.g. Sciffer and Waters, 2002, Lysak, 2004, Sciffer et al., 2005, Ozeke et al., 2009, Lysak et al., 2013, Waters et al., 2013). The work presented here shows that the Buchsbaum resonance may further complicate EMIC wave propagation in the inner magnetosphere. The model, which agrees with Swarm satellite observations, clearly shows wave power from a single equatorial source splitting into two intense channels due to Buchsbaum resonant reflection. The primary channel travels straightforwardly down the field line, reaching the ionosphere at a similar L-shell to the source region. Meanwhile, significant wave energy travels along a more complex pathway: (1) Buchsbaum resonant reflection of waves towards the equator in both hemispheres, (2) inter-hemispheric interference of these reflected wavefronts generating a coherent driver, which (3) pumps energy into a FLR, to form a secondary field-guided channel of wave energy towards the ionosphere. This secondary channel does not correspond to the L-shell of wave origin, but may reach similar intensities to the primary channel.

This study demonstrates the importance of considering Buchsbaum resonant interactions for understanding the complex dynamics of EMIC wave power transfer from an equatorial generation region in the magnetosphere to the ionosphere, and which are important considerations at LEO and may explain recent satellite observations of low-L EMIC waves (e.g. Gamayunov et al., 2018). Given the ongoing interest in assessing the potential role of EMIC waves for the loss of relativistic electrons from the radiation belts as a result of wave scattering into the atmosphere (e.g., Millan and Thorne, 2007), the novel propagation pathway presented here may have broader impacts for space weather as well as in general for understanding instabilities in multi-ion plasmas (e.g. Stenzel et al., 2016).

Data Availability Statement

The ESA Swarm data can be obtained from the ESA server at swarm-diss.eo.esa.int. Van Allen Probes EMFISIS data may be obtained from https://emfisis.physics.uiowa.edu. All equations defining the model are provided in Supporting Information. The CARISMA data is available online at www.carisma.ca.

Acknowledgements

This work was carried out under a programme of, and funded by, the European Space Agency, in the frame of the ESA Living Planet Fellowship “Swarm Investigation of the Energetics of Magnetosphere-Ionosphere Coupling (SIEMIC).” The view expressed in this publication can in no way be taken to reflect the official opinion of the European Space Agency. The work was also supported in part by the Canadian Space Agency (CSA) Class Grant “What role do Alfvén waves play in energy transfer in the dynamical magnetosphere-ionosphere system?” IRM is supported by a Discovery Grant from Canadian Natural Sciences and Engineering Research Council (NSERC). DS is supported by the Canadian Space Agency (CSA). The ESA Swarm data can be obtained from the ESA server at swarm-diss.eo.esa.int. The authors thank D.K. Milling and the CARISMA team for data. CARISMA is operated by the University of Alberta, funded by the Canadian Space Agency; data is available at www.carisma.ca.

References

Balikhin, M. A., deWit, T. D., Alleyne, H. S. C. K.,Woolliscroft, L. J. C.,Walker, S. N., Krasnosel’skikh, V., Mier-Jedrzejeowicz,W. A. C., and Baumjohann, W. (1997). Experimental determination of the dispersion of waves observed upstream of a quasi-perpendicular shock, Geophys. Res. Lett., 24, 787–790.

Barbosa, D. D. (1982), Multi-Ion Resonances in Finite Temperature Plasma, The Astrophysical Journal, 254, 376-390, doi: 10.1086/159742.

Bilitza, D. (2018), IRI the International Standard for the Ionosphere, Adv. Radio Sci., 16, 1-11, https://doi.org/10.5194/ars-16-1-2018.

Blum, L. W., Agapitov, O., Bonnell, J. W., Kletzing, C., & Wygant, J. (2016). EMIC wave spatial and coherence scales as determined from multipoint Van Allen Probe measurements. Geophysical Research Letters, 43, 4799–4807. https://doi.org/10.1002/2016GL068799

Blum, L. W., Bonnell, J. W., Agapitov, O., Paulson, K., & Kletzing, C. (2017). EMIC wave scale size in the inner magnetosphere: Observations from the dual Van Allen Probe. Geophysical Research Letters, 44, 1227–1233. https://doi.org/10.1002/2016GL072316

Buchsbaum, S. J. (1960), Ion resonance in a multicomponent plasma, Phys. Rev. Lett., 5, 495–497.

Friis-Christensen, E., Lühr, H., Knudsen, D., & Haagmans, R. (2008). Swarm—An Earth observation mission investigating geospace. Advances in Space Research, 41(1), 210–216. https://doi.org/10.1016/j.asr.2006.10.008

Gallagher, D.L., P.D. Craven, and R.H. Comfort (2000), Global core plasma model, J. Geophys. Res. 105, A8, 18 819 - 18 833, https://doi.org/10.1029/1999JA000241.

Gamayunov, K. V., Min, K., Saikin, A. A., & Rassoul, H. (2018). Generation of EMIC waves observed by Van Allen Probes at low L shells. Journal of Geophysical Research: Space Physics, 123, 8533–8556. https://doi.org/10.1029/2018JA025629

Hedin, A E. (1991), Extension of the MSIS thermosphere model into the middle and lower atmosphere, J. Geophys. Res., 96, 1159–1172, https://doi.org/10.1029/90JA02125.

Heilig, B. and Lühr, H.: Quantifying the relationship between the plasmapause and the inner boundary of small-scale field-aligned currents, as deduced from Swarm observations, Ann. Geophys., 36, 595–607, https://doi.org/10.5194/angeo-36-595-2018, 2018.

Hendry, A. T., Santolik, O., Miyoshi, Y., Matsuoka, A., Rodger, C. J., Clilverd, M. A., et al. (2020). A multi-instrument approach to determining the source-region extent of EEP-driving EMIC waves. Geophysical Research Letters, 47, 7. https://doi.org/10.1029/2019GL086599

Kessell, R. L., N. J. Fox, and M. Weiss (2012), The Radiation Belt Storm Probes (RBSP) and Space Weather, Space Sci. Rev., doi:10.1007/s11214-012-9953-6.

Kim, E.-H., and J. R. Johnson (2016), Full-wave modeling of EMIC waves near the He+ gyrofrequency, Geophys. Res. Lett., 43, 13–21, doi:10.1002/2015GL066978.

Kim, H., Hwang, J., Park, J., Bortnik, J., & Lee, J. (2018a). Global characteristics of electromagnetic ion cyclotron waves deduced from Swarm satellites. Journal of Geophysical Research: Space Physics, 123, 1325–1336. https://doi.org/10.1002/2017JA024888

Kim, H., Hwang, J., Park, J., Miyashita, Y., Shiokawa, K., Mann, I. R., Raita, T., & Lee, J. (2018b). Large-scale ducting of Pc1 pulsations observed by Swarm satellites and multiple ground networks. Geophysical Research Letters, 45, 12,703–12,712. https://doi.org/10.1029/2018GL080693

Kim, H., Shiokawa, K., Park, J., Miyoshi, Y., Hwang, J., & Kadokura, A. (2020). Modulation of Pc1 wave ducting by equatorial plasma bubble. Geophysical Research Letters, 47, e2020GL088054. https://doi.org/10.1029/2020GL088054

Kletzing, C. A., et al. (2013), The Electric and Magnetic Field Instrument Suite and Integrated Science (EMFISIS) on RBSP, Space Sci. Rev., doi:10.1007/s11214-013-9993-6.

Knudsen, D. J., Burchill, J. K., Buchert, S. C., Eriksson, A. I., Gill, R., Wahlund, J.-E.,…Moffat, B. (2017). Thermal ion imagers and Langmuir probes in the Swarm electric field instruments. Journal of Geophysical Research: Space Physics, 122, 2655–2673. https://doi.org/10.1002/2016JA022571

Lysak, R. L. (2004), Magnetosphere-ionosphere coupling by Alfvén waves at midlatitudes, J. Geophys. Res., 109, A07201, doi:10.1029/2004JA010454.

Lysak, R. L., C. L. Waters, and M. D. Sciffer (2013), Modeling of the ionospheric Alfvén resonator in dipolar geometry, J. Geophys. Res. Space Physics, 118, 1514–1528, doi:10.1002/jgra.50090.

Mann, I. R., et al. (2008), The upgraded CARISMA magnetometer array in the THEMIS era, Space Sci. Rev., 141, 413–451.

Mann, I. R., M. E. Usanova, K. Murphy, M. T. Robertson, D. K. Milling, A. Kale, C. Kletzing, J. Wygant, S. Thaller, and T. Raita (2014), Spatial localization and ducting of EMIC waves: Van

Allen Probes and ground-based observations, Geophys. Res. Lett., 41, 785–792, doi:10.1002/2013GL058581.

Mann, I. R., Ozeke, L. G., Murphy, K. R., Claudepierre, S. G., Turner, D. L., Baker, D. N., et al. (2016). Explaining the dynamics of theultra-relativistic third Van Allen radiation belt. Nature Physics, 12(10), 978–983. https://doi.org/10.1038/nphys3799

Mann, I., Ozeke, L., Morley, S. et al. Reply to 'The dynamics of Van Allen belts revisited'. Nat. Phys. 14, 103–104 (2018). https://doi.org/10.1038/nphys4351

Millan, R. M. and Thorne, R. M. (2007). Review of radiation belt relativistic electron losses. . J. Atmos. Sol.-Terr. Phys. 69(3), 362–377, doi: 10.1016/j.jastp.2006.06.019

Olsen N, Friis-Christensen E, Floberghagen R, Alken P, Beggan CD, Chulliat A, Doornbos E, da Encarnac JT, Hamilton B, Hulot G, van den IJssel J, Kuvshinov A, Lesur V, Luehr H, Macmillan S, Maus S, Noja M, Olsen PEH, Park J, Plank G, Puethe C, Rauberg J, Ritter P, Rother M, Sabaka TJ, Schachtschneider R, Sirol O, Stolle C, Thebault E, Thomson AWP, Toefner-Clausen L, Velimsky J, Vigneron P, Visser PN (2013). The Swarm Satellite Constellation Application and Research Facility (SCARF) and Swarm Data Products. Earth Planets Space 65. 1189–1200

Ozeke, L. G., I. R. Mann, and I. J. Rae (2009), Mapping guided Alfvén wave magnetic field amplitudes observed on the ground to equatorial electric field amplitudes in space, J. Geophys. Res., 114, A01214, doi:10.1029/2008JA013041.

Pakhotin, I. P., Walker, S. N., Shprits, Y. Y., and Balikhin, M. A.: Dispersion relation of electromagnetic ion cyclotron waves using Cluster observations, Ann. Geophys., 31, 1437–1446, https://doi.org/10.5194/angeo-31-1437-2013, 2013.

Saikin, A. A., J.-C. Zhang, R. C. Allen, C. W. Smith, L. M. Kistler, H. E. Spence, R. B. Torbert, C. A. Kletzing, and V. K. Jordanova (2015), The occurrence and wave properties of H+-, He+-, and O+-band EMIC waves observed by the Van Allen Probes, J. Geophys. Res. Space Physics, 120, 7477–7492, doi:10.1002/2015JA021358.

Sciffer, M. D., and C. L. Waters, Propagation of ULF waves through the ionosphere: Analytic solutions for oblique magnetic fields (2002), J. Geophys. Res., 107(A10), 1297, doi:10.1029/2001JA000184.

M. D. Sciffer, C. L. Waters, F. W. Menk. Propagation of ULF waves through the ionosphere: Inductive effect for oblique magnetic fields. Annales Geophysicae, European Geosciences Union, 2004, 22 (4), pp.1155-1169. hal-00317294

Sciffer, M. D., Waters, C. L., and Menk, F. W.: A numerical model to investigate the polarisation azimuth of ULF waves through an ionosphere with oblique magnetic fields, Ann. Geophys., 23, 3457–3471, https://doi.org/10.5194/angeo-23-3457-2005, 2005.

Shprits, Y. Y., Subbotin, D. A., Meredith, N. P., and Elkington, S. R. (2008). Review of modeling of losses and sources of relativistic electrons in the outer radiation belt II: Local acceleration and loss, J. Atmos. Solar-Terr. Phys., 70, 1694–1713, doi:10.1016/j.jastp.2008.06.014.

Shprits, Y. Y., et al. (2013), Unusual stable trapping of the ultrarelativistic electrons in the Van Allen radiation belts, Nature Phys., doi:10.1038/nphys2760.

Shprits, Y., Horne, R., Kellerman, A. et al. The dynamics of Van Allen belts revisited. Nat. Phys. 14, 102–103 (2018). https://doi.org/10.1038/nphys4350

R. L. Stenzel (2016) Whistler waves with angular momentum in space and laboratory plasmas and their counterparts in free space, Advances in Physics: X, 1:4, 687-710, DOI: 10.1080/23746149.2016.1240017

Sydorenko, D., and R. Rankin (2012), Simulation of ionospheric disturbances created by Alfvén waves, J. Geophys. Res., 117, A09229, doi:10.1029/2012JA017693.

Sydorenko, D., and R. Rankin (2013), Simulation of O+ upflows created by electron precipitation and Alfvén waves in the ionosphere, J. Geophys. Res. Space Physics, 118, 5562–5578, doi:10.1002/jgra.50531.

Usanova, M. E., Mann, I. R., Rae, I. J., Kale, Z. C., Angelopoulos, V., Bonnell, J. W., et al. (2008). Multipoint observations of magnetospheric compression-related EMIC Pc1 waves by THEMIS and CARISMA. Geophysical Research Letters, 35, L17S25. https://doi.org/10.1029/2008GL034458

Usanova, M. E., et al. (2010), Conjugate ground and multisatellite observations of compression-related EMIC Pc1 waves and associated proton precipitation, J. Geophys. Res., 115, A07208, doi:10.1029/2009JA014935.

Waters, C. L., Lysak, R. L., & Sciffer, M. D. (2013). On the coupling of fast and shear Alfvén wave modes by the ionospheric hall conductance. Earth, Planets and Space, 65(5), 385-396. https://doi.org/10.5047/eps.2012.08.002

Geophysical Research Letters

Supporting Information for

Novel EMIC Wave Propagation Pathway Through Buchsbaum Resonance and Inter-Hemispheric Wave Interference: Swarm Observations and Modelling

I. P. Pakhotin[1, 2], I.R. Mann[1], D. Sydorenko[1], R. Rankin[1]

[1] Department of Physics, University of Alberta, Edmonton, Alberta, Canada

[2] Department of Physics and Astronomy, University of Calgary, Calgary, Alberta, Canada

Contents of this file

Text S1
Figures S1 to S5
Captions for Movies S1 and S2

Additional Supporting Information (Files uploaded separately)

Movies S1 and S2

Introduction

This Supporting Information contains further material in support of the conclusions of our paper. We provide additional details and description of the simulation model used in the publication, and present movies showing the evolution of the wave energy over time, both in the transverse and compressional B-field components, after the model is initialized with the assumed plasma parameters detailed in the publication. In relation to the Swarm data analysis, it contains figures which further develop on the phase differencing analysis applied to the compressional magnetic field in the Swarm data utilized in the publication to assess the location of the inferred source regions for the waves. It further shows data from Van Allen Probe B and the CARISMA ground magnetometer array (www.carisma.ca) which augment the Swarm A and C observations.

Text S1.

Equations solved by the numerical model

The model uses spherical coordinates and resolves variations along r and ϑ. Periodicity in the azimuthal direction is assumed with all non-stationary values proportional to $\exp{(im\varphi)}$, where m is an integer azimuthal wavenumber. The simulation domain is a sector in the meridional plane with $\vartheta_{min} < \vartheta < \vartheta_{max}$ and $R_E < r < r_{max}$, where R_E is the Earth radius and r_{max} is the radius of the outer boundary. It is assumed that azimuthal variations of wave perturbations are described as $\exp{(im\varphi)}$ where integer m is the azimuthal wavenumber. The model uses dipole geomagnetic field. The ions (H^+, He^+, N^+, O^+, NO^+, and O_2^+) and electrons are represented as fluids. Collisions with neutrals (H, He, N, O, N_2, NO, O_2) are accounted for all charged species. Initial densities and temperatures of electrons, ions, and neutrals are obtained using IRI, GCPM, and MSIS models. The model solves Maxwell equations

$$\frac{\partial \vec{B}}{\partial t} = -\nabla \times \vec{E}\ , \frac{1}{c^2}\frac{\partial \vec{E}}{\partial t} = \nabla \times \vec{B} - \mu_0 \vec{J}\ .$$

The simulation domain includes the air gap between the Earth surface and the bottom of ionosphere, $R_E < r < R_{ion}$, where R_{ion} is the radius of the bottom of the ionosphere. In this gap, the plasma density and the electric current in Ampere's law are zero. In the ionosphere and magnetosphere, the electric current is

$$\vec{J} = \vec{J}_i + \vec{J}_{e,\perp} + \vec{J}_{e,\parallel} + \vec{J}_{ext}$$

where $\vec{J}_i = e\sum_s n_s \vec{u}_s$ is the electric current due to ions, n_s and $\vec{u}_s$ are the density and velocity of ion species s, $\vec{J}_{e,\perp}$ and $\vec{J}_{e,\parallel}$ are the electric currents due to electrons perpendicular and parallel to the geomagnetic field, respectively, $\vec{J}_{ext}$ is the external current driving the wave.

The ion flow velocity is obtained from the linear motion equation

$$\frac{\partial \vec{u}_s}{\partial t} = \frac{e}{m_s}\left(\vec{E} + \vec{u}_s \times \vec{B}_0\right) - \nu_s \vec{u}_s$$

where $\vec{B}_0$ is the geomagnetic field, ν_s is the frequency of collisions with neutrals.

The transverse electron current is due to Pedersen and Hall drifts and is calculated as

$$\vec{J}_{e,\perp} = \bar{\bar{R}}\bar{\bar{\sigma}}_{e,\perp}\bar{\bar{R}}^T\vec{E},\ \bar{\bar{\sigma}}_{e,\perp} = \begin{pmatrix} \sigma_{P,e} & -\sigma_{H,e} & 0 \\ \sigma_{H,e} & \sigma_{P,e} & 0 \\ 0 & 0 & 0 \end{pmatrix},\ \bar{\bar{R}} = \begin{pmatrix} 0 & b_\vartheta & b_r \\ 0 & -b_r & b_\vartheta \\ 1 & 0 & 0 \end{pmatrix},$$

where $\sigma_{P,e}$ and $\sigma_{H,e}$ are the electron Pedersen and Hall conductivities, respectively, defined below, b_r and b_ϑ are the components of a unitary vector $\vec{b}$ directed along the dipole geomagnetic field. Matrix $\bar{\bar{R}}^T$ transforms a vector in the spherical coordinate system $\{\hat{r}, \hat{\vartheta}, \hat{\varphi}\}$ into a coordinate system with basis vectors $\{\hat{x}_1, \hat{x}_2, \hat{x}_3\}$ where $\hat{x}_3 = \vec{b}$, $\hat{x}_2 = \vec{b} \times \hat{\varphi} / |\vec{b} \times \hat{\varphi}|$, $\hat{x}_1 = \hat{x}_2 \times \hat{x}_3$. Matrix $\bar{\bar{R}}$ performs the inverse transformation.
The parallel electron current $\vec{J}_{e,\parallel} = -en_e \vec{u}_{e,\parallel}$ is calculated with the parallel electron velocity defined by the linear dynamics equation

$$\frac{\partial \vec{u}_{e,\parallel}}{\partial t} = -\frac{e}{m_e} \vec{b}(\vec{b} \cdot \vec{E}) - \nu_e \vec{u}_{e,\parallel},$$

where n_e is the electron density and ν_e is the frequency of electron collisions with neutrals.
In the very bottom of the ionosphere, where the collision frequencies are the largest, the electric current is calculated using the conductivity tensor

$$\vec{J} = \bar{\bar{R}} \bar{\bar{\sigma}} \bar{\bar{R}}^T \vec{E}, \ \bar{\bar{\sigma}} = \begin{pmatrix} \sigma_P & -\sigma_H & 0 \\ \sigma_H & \sigma_P & 0 \\ 0 & 0 & \sigma_\parallel \end{pmatrix},$$

where $\sigma_P = \sigma_{P,e} + \sum_s \sigma_{P,s}$ is the total Pedersen conductivity, $\sigma_H = \sigma_{H,e} + \sum_s \sigma_{H,s}$ is the total Hall conductivity, $\sigma_\parallel = \sigma_{\parallel,e} + \sum_s \sigma_{\parallel,s}$ is the total conductivity in the parallel direction. For a charged species α (electrons or ions) $\sigma_{P,\alpha} = \frac{n_\alpha q_\alpha}{B_0} \frac{\omega_{c,\alpha} \nu_\alpha}{\nu_\alpha^2 + \omega_{c,\alpha}^2}$, $\sigma_{H,\alpha} = -\frac{n_\alpha q_\alpha}{B_0} \frac{\omega_{c,\alpha}^2}{\nu_\alpha^2 + \omega_{c,\alpha}^2}$, $\sigma_{\parallel,\alpha} = \frac{n_\alpha q_\alpha}{B_0} \frac{\omega_{c,\alpha}}{\nu_\alpha}$, $\omega_{c,\alpha} = \frac{q_\alpha B_0}{m_\alpha}$, $q_\alpha = -e$ for electrons (subscript $\alpha = e$) and $q_\alpha = e$ for ions (subscript $\alpha = s$).
The boundary conditions are $E_{\vartheta,\varphi}(R_E) = 0$, $B_{r,\varphi}(\vartheta_{min,max}, r < R_{ion}) = 0$, $\vec{B}(\vartheta_{min,max}, r \geq R_{ion}) = 0$, $\vec{B}(r_{max}) = 0$.

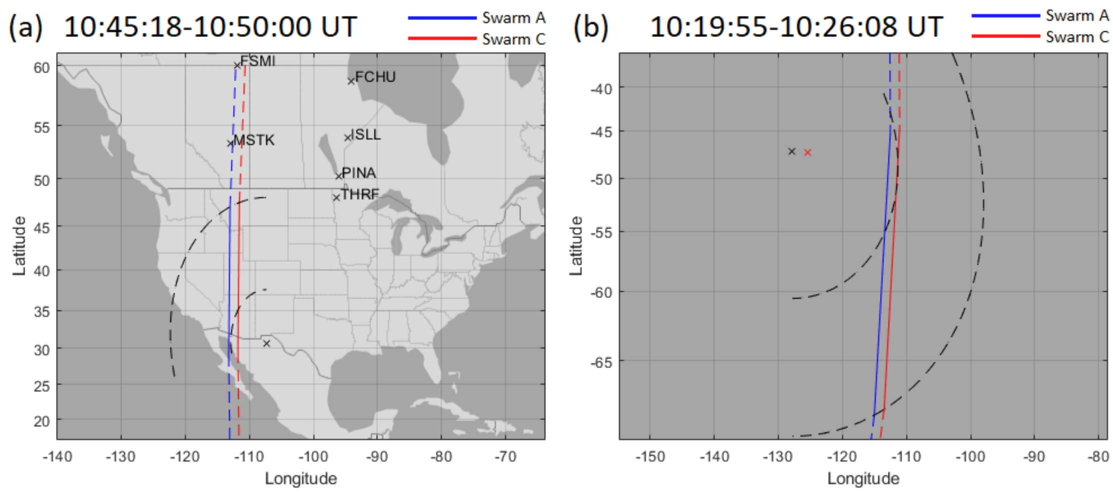

Figure S1. Signal source inference using the phase differencing methodology, as in Figure 1, but without assuming circular propagation of wave fronts. Assuming the Alfven speed does not strongly vary azimuthally between ~5-10 degrees of longitude in this MLT sector, the eccentricity of the ellipse is determined by the ratio of the Alfven speed observed by Swarm A at the point of maximum Swarm A/C phase difference, and the average Alfven speed observed by Swarm A between the point of maximum Swarm A/C phase difference and zero Swarm A/C phase difference. This is applied for both the northern (a) and southern (b) hemispheres. In both cases the ratio is ~0.63. The Alfven speed is estimated using observed magnetic fields, electron density locally from the Langmuir probe on Swarm A assuming a pure O+ plasma. The estimated propagation wave fronts in the areas of interest are plotted as dashed black curves. The ellipse is placed such that its tangent at the point of intersection with Swarm A/C is normal to the Swarm A/C inter-spacecraft separation vector at the point of max phase, and normal to the separation vector at the point of zero phase. The estimated source location is denoted by a black cross; the magnetically conjugate point from the northern hemisphere to the southern hemisphere is denoted by a red cross. A full analysis would require detailed ray tracing, and this is considered to be beyond the scope of this letter.

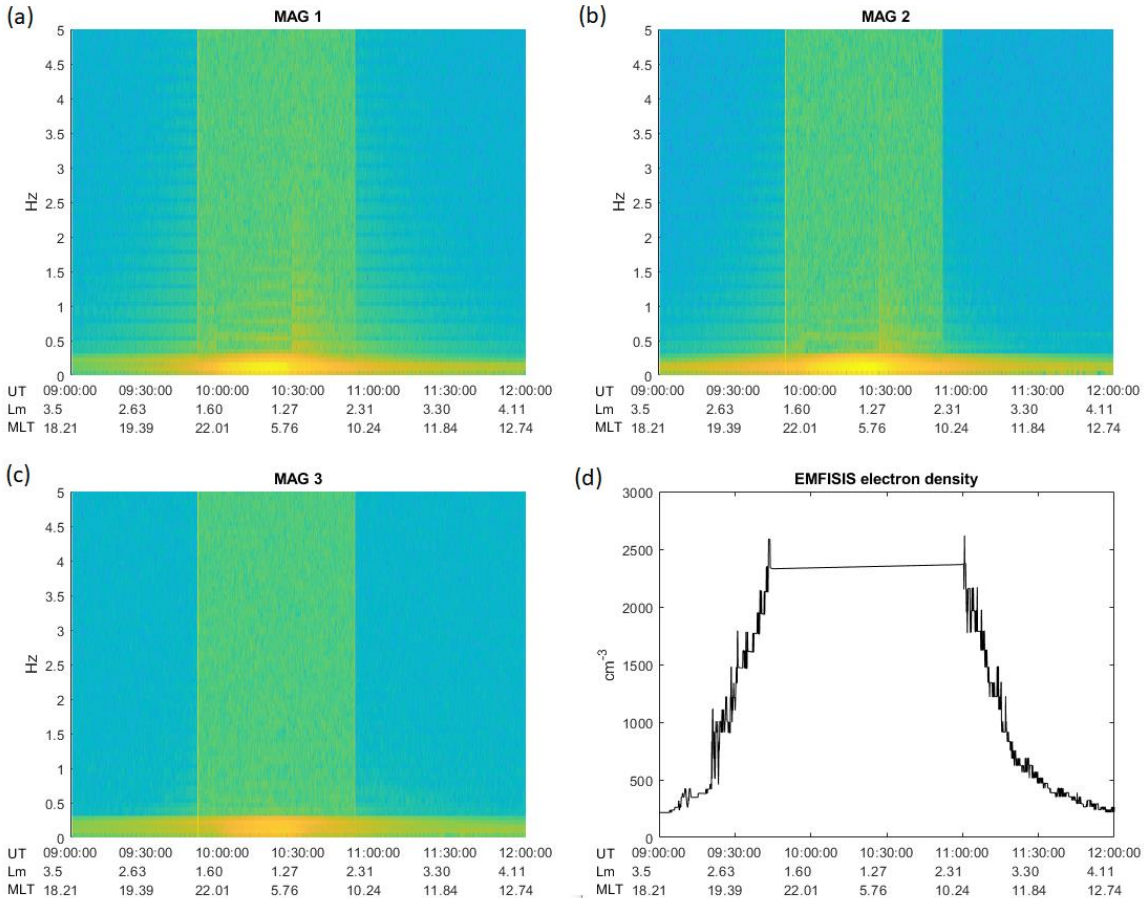

Figure S2. Van Allen Probe B magnetic field dynamic power spectra, with the B-field in MAG coordinates MAG_1 (a), MAG_2 (b) and MAG_3 (c), as well as EMFISIS electron density data (d). The strong emission lines around 0.1 Hz in (a-c) are an artefact of spacecraft spin. No significant EMIC wave activity is detected around 1.5 Hz.

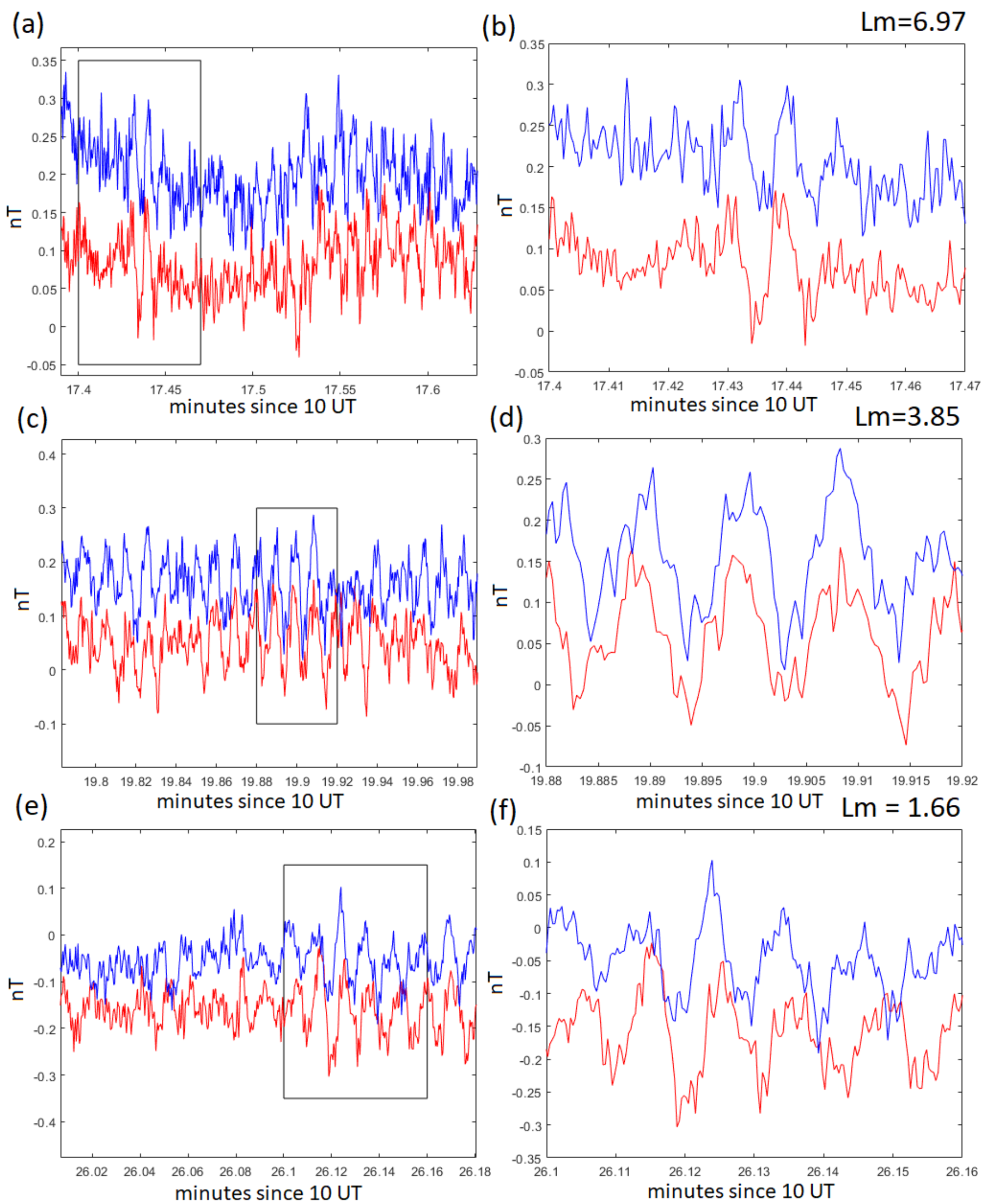

Figure S3. Magnetic field modulus |B| readings for three time periods on Swarm A (blue) and Swarm C (red) as they traversed the southern hemisphere (similar to Figure 3 for the northern hemisphere), the two time series being offset by 0.1 nT for easier viewing. The right column focuses on the areas denoted in the black squares in the left column. In particular, panels (a) and (b) show the period when the wave arrived at the leading Swarm C before Swarm A, panels (c) and (d) show the zero-phase period, while (e) and (f) show the period where the wave first arrives at the westwards Swarm A and the phase difference is maximum at that point.

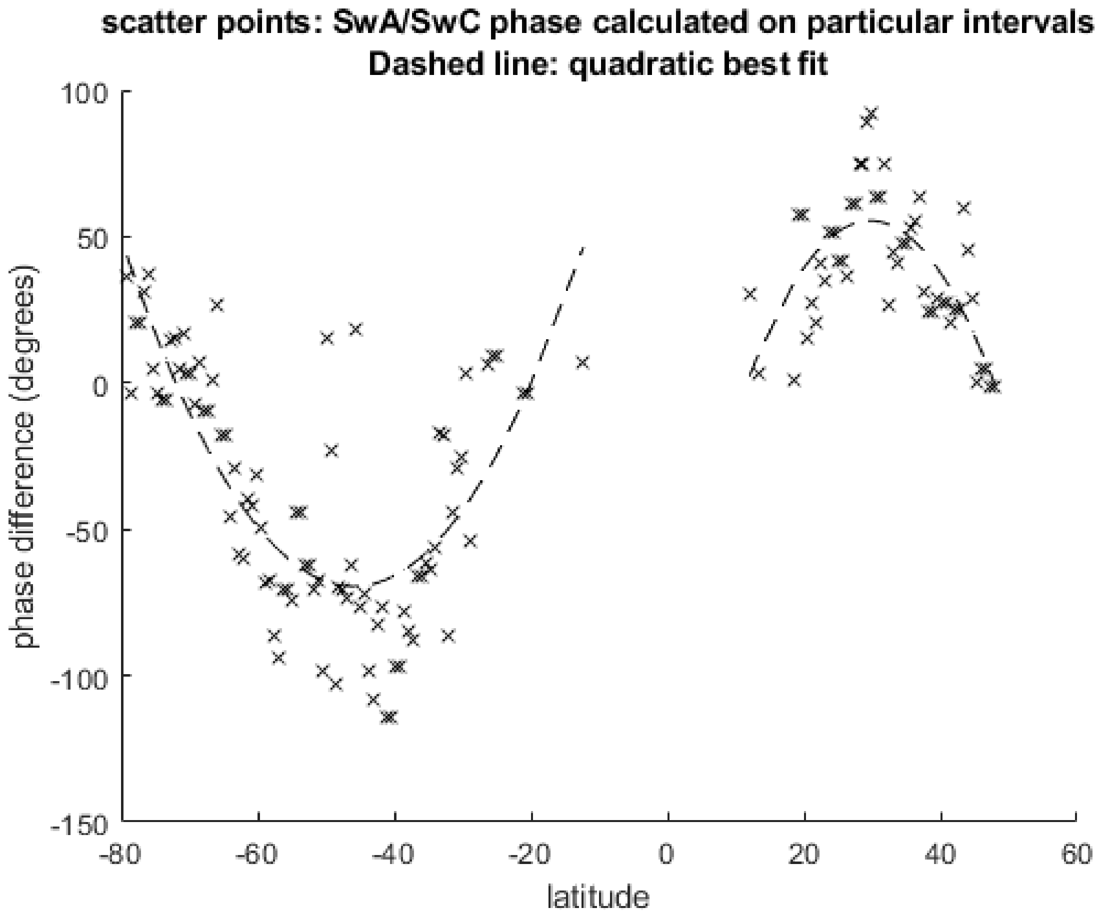

Figure S4. Scatter plot of phase difference between Swarm A and C compressional magnetic field perturbations over a sliding window, as a function of geographic latitude. The dashed lines represent quadratic fits. The plot shows the consistency of the observations with a local source, and with no phase wrap in phase difference between the two spacecraft along their trajectories.

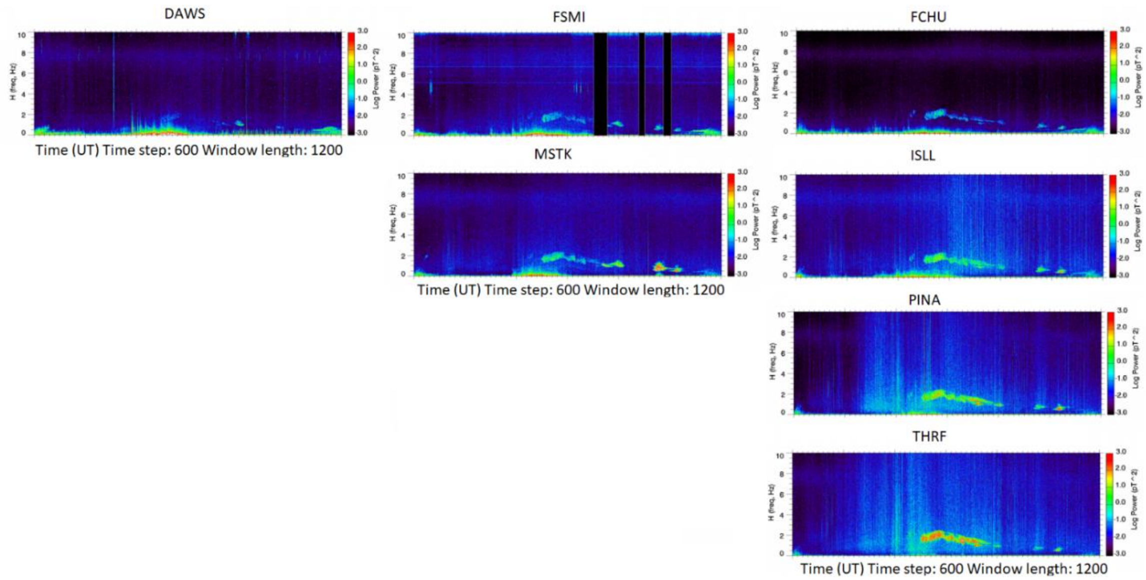

Figure S5. Wave power (H-component) observed at various CARISMA ICM ground stations. The panels are deliberately arranged to reflect the relative geographic position (in latitude and longitude) of the ground stations: lower-latitude ground stations are near the bottom; westwards ground stations are further to the left. It can be seen that wave power is stronger at lower latitudes.

Movie S1. This video shows high-resolution simulation run showing the evolution of the azimuthal magnetic field perturbation in space and time, with the source located in the equatorial plane at 20 x 10^3 km geocentric distance.

Movie S2. This video shows high-resolution simulation run showing the evolution of the $\delta|B|$ in space and time, assuming the source is located in the equatorial plane at 20 x 10^3 km geocentric distance.